Full paper

# Structural figure-of-merits of triboelectric nanogenerators at powering loads

Jiajia Shao[a,b,1], Tao Jiang[a,b,1], Wei Tang[a,b,1], Xiangyu Chen[a,b], Liang Xu[a,b], Zhong Lin Wang[a,b,c,*]

[a] CAS Center for Excellence in Nanoscience, Beijing Key Laboratory of Micro-nano Energy and Sensor, Beijing Institute of Nanoenergy and Nanosystems, Chinese Academy of Sciences, Beijing 100083, China
[b] College of Nanoscience and Technology, University of Chinese Academy of Sciences, Beijing 100049, People's Republic of China
[c] School of Materials Science and Engineering, Georgia Institute of Technology, Atlanta, GA 30332-0245, United States

## ARTICLE INFO

## ABSTRACT

Harvesting mechanical energy and effectively converting it into electrical power by triboelectric nanogenerators (TENGs) have been demonstrated as a burgeoning field of research, that can be essential for the energy of the new era, which is the era of internet of things, big data, and artificial intelligence. Here the structural figure-of-merits (FOM$_S$) for quantitatively evaluating and comparing the output performance of TENGs under different load resistances are studied. Firstly, we introduce the triboelectric process and transient process to analyze the charges transfer in each half cycle. Because each process corresponds to a first-order differential equation, four basic governing equations in a whole cycle are built up. After solving these equations, the real-time output characteristics of TENG are demonstrated, which comprehensively reveal the output behavior of TENG devices. Then, same method is utilized to investigate the maximum harvested energy and structural FOM$_{RS}$ with different load resistances at various maximum displacements. These theoretical results especially about the derived FOM$_{RS}$ provide an improved capability of comparing different configurations of TENGs. This work can not only completely explain the working principles of TENGs, but also enhance the applicability of structural FOM$_{RS}$, enabling more efficient design and optimization of various TENG structures in practical applications.

## 1. Introduction

The phenomenon of triboelectrification caused by contacting/rubbing between two different materials is universal in people's daily life, which is generally considered to be valueless and avoided as much as possible [1–3]. Recently, using this triboelectric effect, triboelectric nanogenarator (TENG) has been invented by Wang's group, which has quickly expands into a fast growing field of research and applications [4,5]. As a sustainable power source, TENG has shown outstanding potential in environmental monitoring, biomedical science, internet of things as self-powered sensors, and it can also be integrated with other types of devices such as mass spectrometer and solar cells [6–12]. The theoretical origin of TENG is Maxwell's displacement current, which is generated by horizontal/vertical movement of the triboelectric layers with opposite charges on contact surfaces [13,14]. When the tribo-electric layers are driven by a periodic time-varying mechanical force, the electric field caused by those charges is also changing with time. Subsequently the time-varying electric field produces displacement current inside the materials. In other words, TENGs represent the

application of Maxwell's displacement current in energy and sensors [13]. In fact, ever since the first report of the TENG in 2012 by Wang et al., a few theoretical works have been done on the working mechanism of TENGs [15–21]. In these studies, the TENG can be represented by an ideal voltage source in series with a capacitor, which is modeled through a first-order lumped-parameter equivalent-circuit model [22,23]. However, the real-time output characteristics of the TENG in an entire cycle, such as the transferred charges, current, and voltage, have not been systematically studied.

Moreover, many types of TENGs with different configurations have been developed to accommodate practical applications [24–30]. There are four basic working modes, i.e., lateral sliding (LS) mode, single-electrode (SE) mode, vertical contact-separation (CS) mode, and free-standing triboelectric-layer (CFT) mode [31–34]. Each mode defines its own structure and can choose various triboelectric materials, leading to a difficulty to characterize and compare the output performance. Zi et al. have proposed a structural figure-of-merit to solve mentioned problems, but it is still limited in some way [35]. The upper bound for power output was calculated by the product of open-circuit voltage

---

($V_{OC}$) and short-circuit charges ($Q_{SC}$) in an operation cycle, which is not realistic in practice if TENG is connected to an external load. Because the practical output under a load resistance is significantly lower than that of the calculation from the short-circuit process. It is inaccurate to evaluate the output performance of TENGs with different load resistances. Besides, the device figure of merit ($FOM_{device}$) has been derived by Peng et al. recently [36]. However, the edge effect as a vital factor has not been taken into account, resulting in a relatively low accuracy in practical applications. Therefore, deriving more practical and operational figure-of-merit is highly desired for TENGs.

In this manuscript, the structural figure-of-merits ($FOM_S$) under various load resistances are proposed to compare and evaluate the different TENG architectures. Firstly, based on the working principle of TENGs, the triboelectric process and transient process are introduced to describe the charges transfer in every half cycle of TENGs. Owing to each process corresponds to a first-order differential equation, four different governing equations are derived in one cycle. After solving these equations, circuit variables such as charge $Q(t)$, current $I(t)$, voltage $V(t)$, and power $P(t)$ as functions of time are obtained, and then we systematically discuss the maximum possible output energy ($E_m$) and related $FOM_S$ at various load resistances. Most importantly, through the calculated $FOM_{RS}$ under optimum resistance ($R_{opt}$) at different maximum displacement $x_{max}$, we can compare and evaluate the TENGs with different structures accurately and comprehensively. In short, the structural $FOM_{RS}$ calculated with different load resistances, allows precise determining of the maximum energy output for all TENG structures, therefore, it has significant potential to be an essential tool in optimizing TENG designs for energy harvesting and mobile electronics applications.

## 2. Results and discussion

### 2.1. Deriving the governing equations for TENGs

A typical structure of TENG is composed of two electrodes and at least one dielectric material layer, which can be regarded as a parallel plate capacitor. When there is a periodic driven force that separates the triboelectric pairs with opposite charges, the original electrostatic equilibrium is broken, leading to a time-varying voltage across the TENGs. The potential difference drives the charges to flow through an external load, resulting in an AC signal, thus generating the harvested energy. Fig. 1 illustrates a LS mode TENG used in this work, and a complete response of the circuit variables in an entire cycle. Like a sequential switching in a conventional $RC$ circuit, four steps can be divided in one cycle (Fig. 1a). For the step I, the sliding part moves from $x = 0$ to $x = x_{max}$, and the potential difference drives some charges to the stationary electrode (Metal 2). The time needed is longer than that in short circuit state, so that just part of the energy can be harvested during the relative motion between the triboelectric layers. For the step II, the sliding part stops at $x = x_{max}$, and the TENG can be considered as a parallel plate capacitor, because of its built voltage across the capacitor (TENG). The voltage cannot drop to 0 V instantaneously, so that the charges can flow to the stationary electrode continuously until the electric filed is balanced. In other words, all of the triboelectric charges can be transferred from the top electrode (Metal 1) to the stationary electrode. Based on electrical circuit theory, the trends of charges and other variables at step II are similar to those of zero input response in a conventional $RC$ circuit, thus these responses are referred to as the transient process [36,37]. In general, TENGs have to experience such process under a periodic mechanical motion. The time needed in this transient period mainly depends on the product of the external load and capacitance of the TENG, which will be discussed latter. As a result, each half cycle of TNEGs can be divided into two processes: triboelectric process and transient process, which can be used to analyze the variables during the remaining half cycle as well. Therefore, in one whole cycle the triboelectric process contains the step I and III, while

the step II and IV belong to the transient process, enabling a better understanding of the working mechanism of the device.

To investigate the circuit variables in an operation cycle, the transferred charges as a function of time $Q(t)$ were applied to derive the governing equation. Since the differential equations are all the first-order, the circuit here is called as first-order circuit. According to Gauss' law and Kirchhoff's law, four different governing equations were provided to describe the circuit variables of the LS mode TENG (Supplementary session 1), which can be given by

$$R\frac{dQ}{dt} = -\frac{d_0 Q}{w\varepsilon_0(l - x(t))} + \frac{\sigma x(t)d_0}{\varepsilon_0(l - x(t))}\left(0 \leq t < t_1, t_1 = \frac{x_{max}}{v}\right), \quad \text{Step I}$$

(1)

$$R\frac{dQ}{dt} = -\frac{d_0 Q}{w\varepsilon_0(l - x_{max})} + \frac{\sigma x_{max} d_0}{\varepsilon_0(l - x_{max})}\left(t_1 \leq t < t_2, t_2\right.$$

$$= t_1 + 5\tau_1\Bigg), \quad \text{Step II}$$

(2)

$$R\frac{dQ}{dt} = -\frac{d_0 Q}{w\varepsilon_0(l - x(t - t_2 + t_1))}$$

$$+ \frac{\sigma x(t - t_2 + t_1)d_0}{\varepsilon_0(l - x(t - t_2 + t_1))}\left(t_2 \leq t < t_3, t_3 = t_2 + \frac{x_{max}}{v}\right), \quad \text{Step III}$$

(3)

$$R\frac{dQ}{dt} = -\frac{d_0 Q}{w\varepsilon_0 l}\left(t_3 \leq t < t_4, t_4 = t_3 + 5\tau_2\right), \quad \text{Step IV}$$

(4)

Here, $\sigma$ is the surface charge density, $v$ is the sliding speed, $x$ and $x_{max}$ represent the relative displacement and maximum separation distance, respectively. $d_0$ is a thickness constant defined as $d_1/\varepsilon_1$, and $d_1$, $\varepsilon_1$, $l$, $w$ are the thickness, relative dielectric constant, length and width of the dielectric layer, respectively, which determine the inherent capacitances of TENGs. Especially, $\tau_1$ and $\tau_2$ (for the steps II and IV) are the time constant, denoted by

$$\tau_1 = \frac{Rw\varepsilon_0(l - x_{max})}{d_0}$$

(5)

$$\tau_2 = \frac{Rwl\varepsilon_0}{d_0}$$

(6)

The time constant is an important parameter for the first-order circuits, which is equivalent to the product of the resistance and capacitance of TENGs. Here it is used to describe the changes of the circuit variables and simplify the governing equations during the transient process.

With the initial boundary condition of $Q(t = 0) = 0$, the transferred charges in one cycle can be calculated by solving Eqs. (1)–(4) (Supplementary session 1). We note that the solutions for governing Eq. (1) have been discussed in detail by previous researches, but the rest parts (Eqs. (2)–(4)) have never been clearly analyzed [15–18]. Taking Eq. (2) as an example, the analytic expressions of $Q(t)$, $I(t)$, $V(t)$, and $P(t)$ were derived and simplified as shown in Supplementary session 2. It is obvious that these circuit variables decay exponentially with the increase of time. The time constant $\tau$ or the $RC_{xmax}$ ($C_{xmax}$ represents the total capacitance at $x = x_{max}$) determines the rate at which those circuit variables approach to zero. Using the concept of time-constant, we simplify these expressions for current, voltage, and power during the transient process (at step II) as

$$I_2(t) = I_1 \exp(-t/\tau_1)$$

(7)

$$V_2(t) = V_1 \exp(-t/\tau_1)$$

(8)

$$P_2(t) = I_1^2 R \exp(-2t/\tau_1)$$

(9)

where $I_1 = I(t = x_{max}/v)$, and $V_1 = V(t = x_{max}/v)$. Generally the time
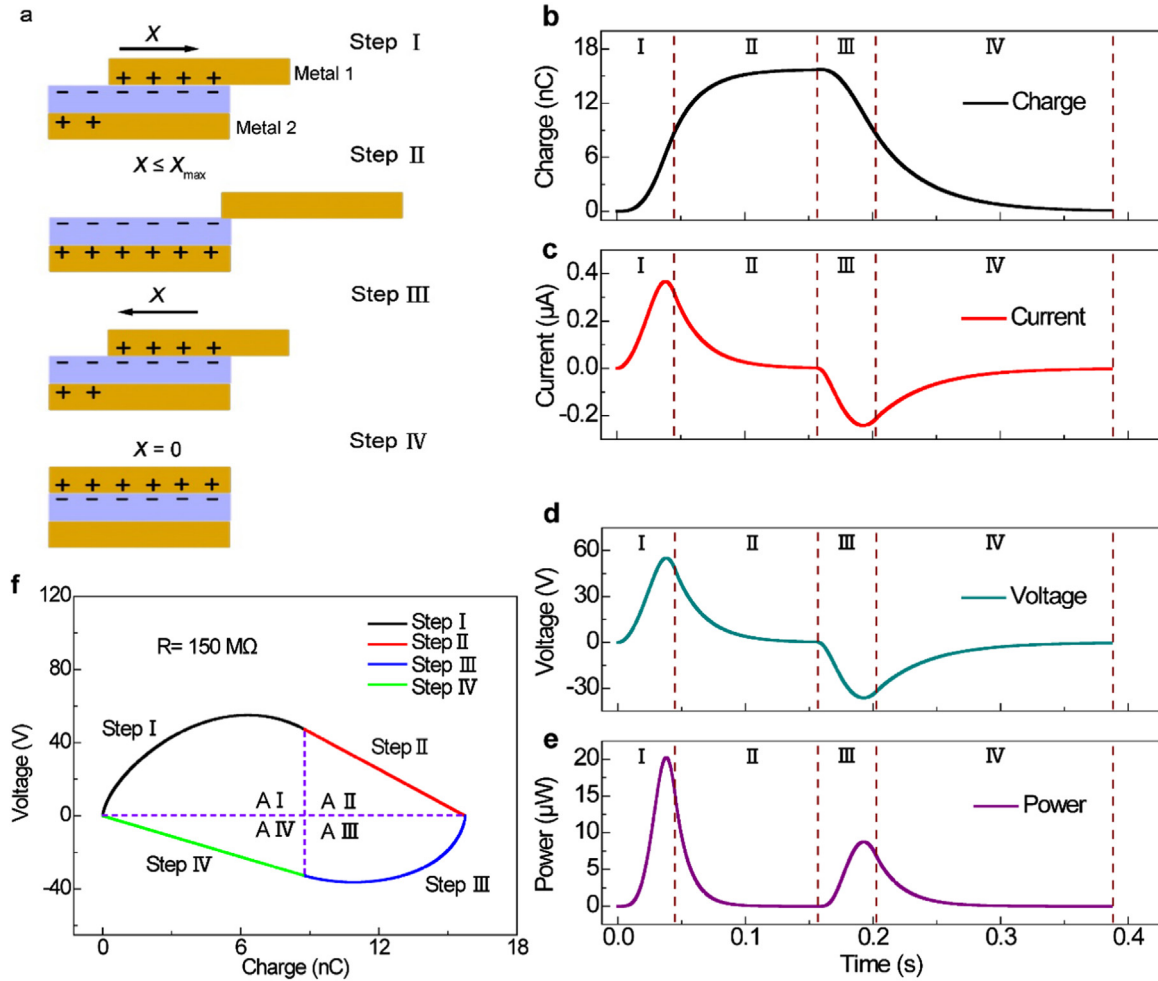
**Fig. 1.** (a) Schematic diagram of a lateral sliding (LS) triboelectric nanogenerator (TENG) with four steps. Step I, the sliding part moves from $x = 0$ to $x = x_{max}$; step II, the sliding part stops at $x = x_{max}$, and residue charges continuously flow from top electrode (Metal 1) to bottom electrode (Metal 2) to maintain electrostatic equilibrium; step III, the sliding part moves reversely from $x = x_{max}$ to $x = 0$; step IV, the sliding part stops at $x = 0$, and the residue charges continuously flow from the bottom electrode to top electrode until the electrostatic equilibrium state, completing an entire cycle. The corresponding times needed during the operational process are $T_1$, $T_2$, $T_3$ and $T_4$, respectively. (b) Charge-time, (c) current-time, (d) voltage-time and (e) power-time relationships with external load resistance of 150 MΩ in one cycle. (f) The voltage-charge (V-Q) plot of the CMEO with external load resistance of 150 MΩ, where the CMEO represents the maximum energy output in one cycle.

constant $t$ ranges from 0 to $5\tau$, because after five time constants, those circuit variables will approach to 0 ($e^{-t/\tau} = e^{-5\tau/\tau} = e^{-5} \approx 0.007$). Taking the changes of voltage across the TENG as an instance, in Eq. (8), the time constant $\tau$ will always have some value due to resistance present in a capacitive network [38]. In some situations, the value of $\tau$ may be very small. Therefore, it can be generally concluded that the voltage across a TENG cannot change instantaneously even the triboelectric layer stops moving suddenly.

The time constant is presented for the first time, so mentioning several of its characteristics is worthwhile. Firstly, one might assume that this constant is very similar to that in a conventional $RC$ circuit. That's because when the sliding part stops, the LS mode TENG can be regarded as a parallel-plate capacitor with the capacitance of $C_{xmax}$ [37]. Connecting with a load resistance, the circuit at the transient process is equivalent to a $RC$ circuit, so that those circuit variables could be all expressed in exponential forms. Moreover, as stated above, it needs five time constants for the circuit variables including current, voltage and power to drop to zero. Specifically, at step II, the initial boundary conditions for the LS mode TENG are $I_1 = I(t = x_{max}/v)$ and $V_1 = V(t = x_{max}/v)$. On the other hand, the time constant at step IV is $\tau_2$, equivalent to the product of $RC_0$, where the $C_0$ represents the capacitance of TENG at $x = 0$. For the same reason, the mentioned

strategies could be applied to analyze the circuit variables of TENGs with different configurations.

Based on the derived equations, the corresponding $Q(t)$, $I(t)$, $V(t)$, and $P(t)$ were numerically calculated under the external load resistance of 150 MΩ in an operation cycle (detailed parameters are shown in Table 1), as shown in Fig. 1b-e. Then, the plots of voltage ($V$) against the transferred charge ($Q$) are built up to show the electrostatic state and energy output of TENGs. It should be noticed that in this ideal system, the total triboelectric charges are not decreased or increased and steady state surface charges $\sigma S$ are established, all of which could pass through the load resistor in each half cycle. The encircled areas of

**Table 1**
Parameters utilized in the theoretical calculation for the LS mode TENG.

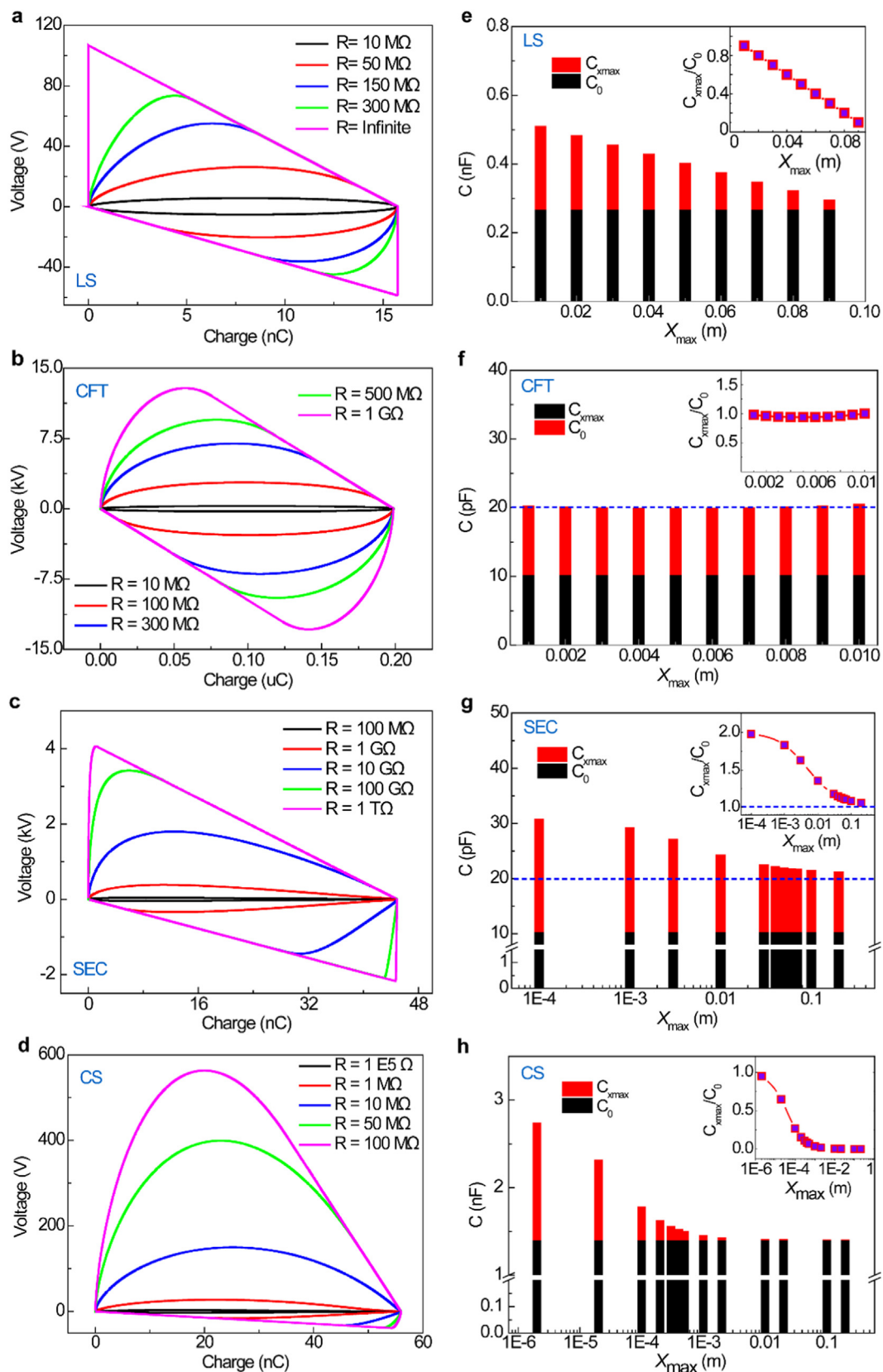| Structure component | Parameter utilized |
|---|---|
| Dielectric effective thickness, $d_0 = \Sigma d_i/\varepsilon_i$ | 165 μm |
| Width of Dielectrics, $w$ | 0.05 m |
| Length of Dielectrics, $l$ | 0.1 m |
| Surface charge density, $\sigma$ | 7 μC m$^{-2}$ |
| Maximum distance, $x_{max}$ | 0.01–0.09 m |
| Velocity, $v$ | 1 m/s |

**Fig. 2.** The CMEO with various external load resistances of (a) LS mode, (b) contact freestanding triboelectric-layer (CFT) mode, (c) single-electrode contact (SEC) mode, and (d) vertical contact-separation (CS) mode TENG. Comparisons of the capacitance $C_{xmax}$ at $x = x_{max}$ and $C_0$ at $x = 0$ of (e) LS mode, (f) CFT mode, (g) SEC mode and (h) CS mode TENG. The insets are the profile of the ratio $C_{xmax}/C_0$.

the *V-Q* plots are equivalent to the maximum output energy per cycle, named as "cycles for maximum energy output" (CMEO). Fig. 1f shows a typical curve of CMEO with a load resistance of 150 MΩ, where AI, AII, AIII, and AIV represent the energy output during the corresponding step, respectively.

## 2.2. Theoretical maximum energy output of TENG

The calculation results under different load resistances of the LS mode TENG were plotted in Fig. 2a. We can observe that the higher the resistance, the higher the output energy per cycle. Therefore, the maximized output energy could be obtained under an infinitely large resistor (R = + ∞), which is equivalent to the product of the maximum open circuit voltage ($V_{OC}$) and short circuit transferred charges ($Q_{SC}$) [35]. In such case the plot of CMEO changes from an oval shape to a trapezoid shape, the vertices of which mainly depends on the maximum positive open-circuit voltage ($V_{OC,max}$, calculated for the first half cycle), the maximum short circuit transferred charges ($Q_{SC,max}$) and negative $V_{OC,max}$ (calculated for the second half cycle). The huge difference between the positive and negative $V_{OC,max}$ is because of the different capacitances. In both cases the total transferred charges are considered equivalent, nevertheless, the former (when $x = x_{max}$) has a smaller capacitance ($C_{xmax}$) while the latter (when $x = 0$, corresponding to the capacitance of $C_0$) is usually larger, resulting in the mentioned phenomena. In general, when $x_{max}$ changes, the $C_{xmax}$ will change correspondingly, but the $C_0$ substantially stays the same (Fig. 2e, the inset is the ratio of $C_{xmax}/C_0$). In addition, to be closer to real conditions, the numerical calculations above are adopted a sinusoidal motion (Supplementary session 3). To compare with the sinusoidal motion, the CMEO for LS mode TENG under a constant velocity was also calculated and shown in Fig. S1 (Supplementary session 4). We found that both cases show almost the similar results under various load resistances. The difference between the positive and negative $V_{OC,max}$ is inversely proportional to the ratio of $C_{xmax}/C_0$, which is consistent with that in the sinusoidal motion.

The strategy of using CMEO to show the output characteristics of LS mode TENG is also suitable for other types of TENG (Fig. 2b–d). The schematic diagrams of other three basic working modes of TENG are depicted in Fig. S2, which are offered to understand the core physics of TENGs. The derived formulae and detailed parameters are shown in Supplementary session 5–7 and Table S1–3. Fig. 2b is a typical symmetry figure of a CFT mode TENG. The exactly same vertices of maximum positive and negative voltages are attributed to the constant capacitance, even the $x_{max}$ changes with the driven force (Fig. 2f). The constant inherent capacitance makes the CFT mode TENG a linear and time-invariant device, which can act as an ideal medium to transform mechanical vibrations to electrical signals, and find wide applications in self-powered systems [18]. Different from the CFT mode, the maximum negative voltage is nearly equal to the half of the maximum positive voltage at a large resistance (1 TΩ) for the SEC mode TENG (Fig. 2c). That's because when *x* arrives at a high enough value (0.4 m), the $C_{xmax}$ and $C_0$ become much close to each other (Fig. 2g), and only half of the triboelectric charges transfer from one electrode to the other one [32]. However, for the CS mode TENG (Fig. 2d, h), we can clearly observe that there is a significant difference between the maximum negative voltage and positive voltage, which is mainly due to the small ratio of $C_{xmax}/C_0$. Because a relatively bigger $C_0$ (compared with $C_{xmax}$) can lead to a lower maximum negative voltage, under the same transfer charges. In particular, when $x_{max}$ reaches 0.1 m, the ratio of $C_{xmax}/C_0$ nearly drops to zero, resulting in the huge difference between the two voltage peaks. These ratios used in Fig. 2a-d are extracted and shown in Fig. S3. The real-time power-time relationships under various resistances for other three basic modes of TENGs are plotted in Fig. S4. It is apparent that there exists an optimum resistance for reaching the maximum power in each model. Therefore, the CMEO plays a key role to describe the output trends of TENGs under different resistances,

confirming that the introduced four steps in an operation cycle are highly applicable as compared with previous methods.

Zi et al. presented one special method to describe the maximum possible output energy ($E_m$) though considering an upper bound of power output, which is constructed with the open-circuit and short-circuit processes. $V_{OC}$ and $Q_{SC}$ are used to define the $E_m$ in a single cycle [35]. However, in general there is no energy output under the SC conditions. More importantly, the practical output limit under a load resistor is usually much lower than that calculated from the product of maximum $V_{OC}$ and $Q_{SC}$. Based on that, we propose a more practical and operable approach to calculate the $E_m$ by considering the real-time power output with different load resistances. As described above, the encircled area by the *V-Q* plot has been divided into four parts, and each part represents the magnitude of output energy in a corresponding step. Therefore, the $E_m$ can be precisely calculated by summing the integral of instantaneous power in every step, which is defined as:

$$E_m = \int_0^{t_1} P_1(t)dt + \int_{t_1}^{t_2} P_2(t)dt + \int_{t_2}^{t_3} P_3(t)dt + \int_{t_3}^{t_4} P_4(t)dt \tag{10}$$

where $P_1$, $P_2$, $P_3$ and $P_4$ represent the instantaneous power at step I, II, III, and IV respectively. In other words, the practical and real-time energy output is equal to the integral of power to the time.

As shown in Fig. 3a-b, the $W_{R1, AI}$, $W_{R2, AII}$, $W_{R3, AIII}$, and $W_{R4, AIV}$ represent the $E_m$ at step I, II, III, and IV, respectively. We noticed that as the load resistance increases, the harvested energy at step I first increases and then decreases, thus generating a energy peak. However, at step II, the output energy has a sudden increase until it reaches a saturation value. Similar phenomenon can also be found at steps III and IV. As a result, during the triboelectric process (including the steps I and III), a harvested energy peak will be presented, while at the transient process (during the steps II and IV), the harvested energy first slightly increases and then increases rapidly until the maximum value (Fig. 3c). As a result, the $E_m$ has a increasing trend with the increase of the load resistance, and then reaches its saturation value at the infinite load resistance, which is very consistent with the enclosed areas of the CMEO demonstrated in Fig. 2. In addition, three other basic working modes of TENGs are employed to calculate the $E_m$, as depicted in Fig. S5–7 (detailed parameters are listed in Table S1–3). It is obvious that those trends under various load resistances are very similar to those of the LS mode TENG. Especially each mode has its own distinctive feature, suggesting a new approach to compare the differences of TENGs. For instance, either at the separation process (at step I and II) or the contact process (at steps III and IV), the $E_m$ of the CFT mode TENG (Fig. S6) is completely equal. Therefore, these results demonstrate that the strategy of calculating $E_m$ through the Eq. (11) is effective and operable.

The unique performance of $E_m$ under different load resistances of TENGs can be interpreted physically. Firstly, during the triboelectric process, when there is a load resistance, the charge transfer rate between the two electrodes will be lower than that at SC condition. If the load resistance is small, the limitation is less so that the charge transfer can catch up with the maximum rate, which is determined by the driving motion. If the load resistance continues to increase, the limitation will be obvious. When there is a large enough resistance, the charge motion would be strongly limited (very small transfer rate), producing a lower energy output. However, when the optimum resistance is loaded or certain resistance is matched with the impedance of the TENG, the mechanical energy could be converted into electric power more effectively, thus generating the harvested energy peak during the triboelectric process [22,36]. Secondly, after the sliding part stops, the TENG can be regarded as a capacitor, and the circuit becomes a *RC* circuit as stated above. It has already been proven that the voltage across the TENG at the transient process cannot be changed immediately. When the load resistance is small, there will be a low voltage and the residue charges in TENG are also few, leading to a lower energy output. Instead, if the load resistance is large, residue charges will be more and the voltage across the TENG would increase, with the
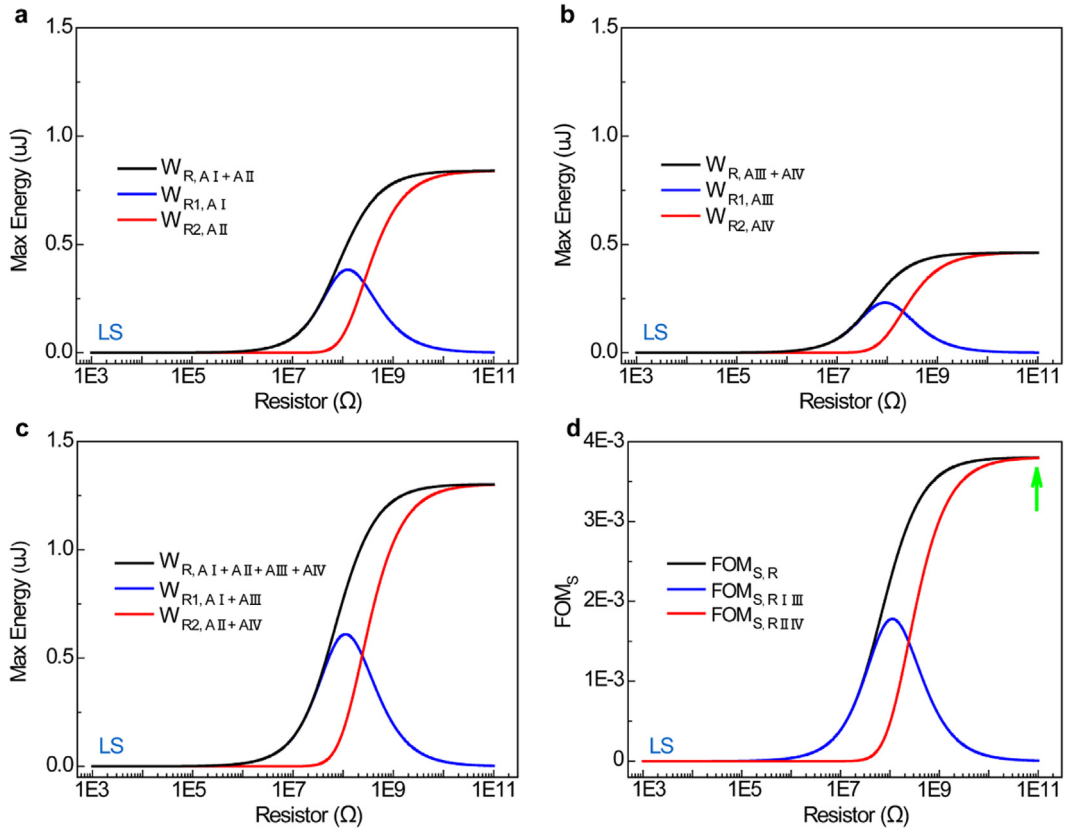
**Fig. 3.** The influences of various external load resistances on the maximum harvested energy ($E_m$) of LS mode TENG. $W_{R1,\ AI}$, $W_{R2,\ AII}$, $W_{R3,\ AIII}$ and $W_{R4,\ AIV}$ represent the corresponding $E_m$ at the steps I, II, III, and IV, respectively. (a) The $E_m$ at the step I and step II ($W_{R,\ AI\ +\ AII}$), (b) the $E_m$ at the step III and IV ($W_{R,\ AIII\ +\ AIV}$), (c) the $E_m$ from one operational cycle ($W_{R,\ AI\ +\ AII\ +\ AIII\ +\ AIV}$). (d) The structural figure-of-merit (FOM) of the LS mode TENG, where the $FOM_{S,R}$ represents the trend of figure-of-merit with different load resistances, $FOM_{S,\ RII\ III}$ and $FOM_{S,\ RII\ IV}$ represent the trends of FOMs at the triboelectric process and transient process, respectively. Green arrow represents the maximum $FOM_{S,R}$ under an infinitely large load resistance.

magnitude of approaching $V_{OC}$. As a result, the harvested energy will be many times higher than that for a small resistor. However, much more time is needed for these residue charges to discharge gradually through the external circuit to reach electrostatic equilibrium, where the discharging time is predicted by the time constant. Therefore, the total $E_m$ by summing each part from the triboelectric process and transient process, has an increasing trend with the increase of load resistance.

On the other hand, we compare the relation and difference between the triboelectric process and transient process. Firstly, there is a time-varying capacitance for the TENGs at the triboelectric process (except for the freestanding mode TENG, whose capacitance is almost constant and independent of $x$) [22,36]. This is because once a relative motion of the triboelectric pairs is introduced by an external driving force, changes of contact area and transferred charges lead to changes of capacitance accordingly. During the transient process, the residue charges in TENGs (could be considered as a capacitor) discharges gradually through the external load, resulting in the decrease of the total capacitance. In addition, the TENG can convert mechanical energy into electrical power immediately and simultaneously. A part of the converted energy is delivered to the loaded resistance during the triboelectric process, and the other part is stored in the TENG as the form of voltage, which can decrease exponentially as the time elapses and finally approach 0 at the transient process. The time needed mainly depends on the time constant denoted by Eqs. (5) and (6). Therefore, ideal TENGs can neither dissipate nor decrease/increase any of the energy, which just converts the mechanical energy into electrical potential energy for distributed power sources.

### 2.3. Structural $FOM_S$ under different load resistances

Figure of merit is a crucial quantitative parameter to evaluate and compare the output characteristics of TENGs with various structures. The FOM is a non-dimensional number which is mainly dependent on the $E_m$ and $x_{max}$, normalized by the charge density $\sigma$, real contact area $A$, and maximum displacement $x_{max}$, which is defined as [35]

$$FOM_S = \frac{2\varepsilon_0}{\sigma^2} \frac{E_m}{Ax_{max}} \tag{11}$$

Unlike the previous report in which the $E_m$ and structural $FOM_S$ were just derived by calculating the product of maximum $V_{OC}$ and $Q_{SC}$ [35]. Here, the $E_m$ and relevant $FOM_S$ were systematically calculated in an operation cycle with various load resistances ranging from zero to infinity (detailed parameters are listed in Table 1), taking the LS mode TENG as an example. In Fig. 3d, the $FOM_{S,R}$, which are composed by the $FOM_{S,\ RI\ III}$ and $FOM_{S,\ RII\ IV}$, represent the change of figure-of-merits at different load resistances; $FOM_{S,\ RI\ III}$ and $FOM_{S,\ RII\ IV}$ stand for the change tendency of FOMs at the triboelectric process and transient process, respectively. We found that the variation tendency of these structural $FOM_{S,R}$ is similar to that of $E_m$ shown in Fig. 3c, just with different scales. For example, the higher the harvested energy outputs, the larger the relevant structural $FOM_{S,R}$ becomes, and there is a peak $FOM_{S,R}$ presented during the triboelectric process either. Note that the green arrow represents the obtained maximum $FOM_{S,R}$ under the load resistance approaching infinity. The $FOM_{S,R}$ for other three basic modes of TNEGs are very similar to that of the LS mode TENG, as demonstrated in Fig. S5–S7. Consequently, we can make a general conclusion that the structural $FOM_S$ calculated under different load resistances can reflect and compare the output characteristics of TENGs with different
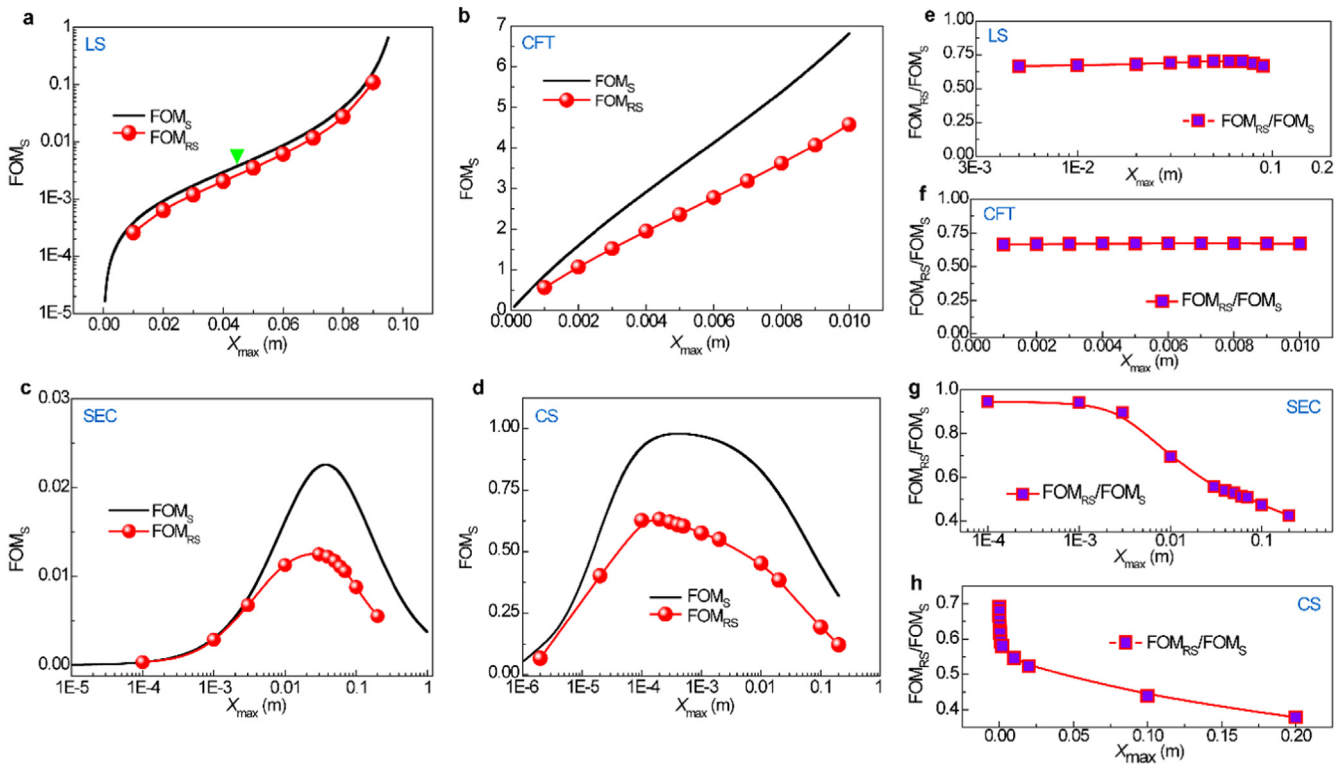
**Fig. 4.** The structural figure-of-merits under optimum resistance (FOM$_{RS}$) for (a) LS mode, (b) CFT mode, (c) SEC mode and (d) CS mode TENG. The black lines represent the FOM$_S$ for the corresponding modes of TENG, which are calculated under infinitely large resistances. The green arrow represents the figure-of-merits calculated at $x_{max}$ = 0.45 m. (e-h) The ratios of FOM$_{RS}$/FOM$_S$ for those basic modes of TENGs.

structures.

The advantage of dividing one operation cycle into four parts to discuss the output performance of TENGs is that this problem can be split into four simpler problems. Combining the four derived governing equations and Eq. (10), we can calculate the $E_m$ and relevant FOM$_S$ when the $x_{max}$ is fixed. Usually the $E_m$ and FOM$_S$ obtained with large resistance are very difficult to verify, because it needs a fairly long time for charges to completely transfer. However, from the point of view of TENG applications, it is more convenient to have the FOM$_S$ that can be used as guidance through the design parameters and optimum resistance. Specifically, we can obtain the matched resistance at a given mechanical motion, and under this matched resistance the mechanical energy can be more effectively converted into electric power. In other words, the $E_m$ and related structural figure-of-merits (FOM$_{RS}$) calculated under optimum resistance are more practical and easily achievable, in comparison with those under other resistances that are larger than the matched resistance. The FOM$_{RS}$ for the four basic modes of TENG with respect to $x_{max}$ were demonstrated and calculated, as depicted in Fig. 4. The detailed parameters and derived formulae are shown in Table S1–3, and Supplementary Session 5 and 8.

From Fig. 4b, we notice that the structural FOM$_{RS}$ of CFT mode TENG is the highest, which is due to its large transferred charge amount caused by the two triboelectric pairs (Fig. S1e). So that this mode is very beneficial to output the largest energy compared to other modes TENGs with the same size and materials, but it is more prone to be influenced by air breakdown effect, leading to suppressed output energy [39]. The minimum FOM$_{RS}$ occurring in the SEC mode (Fig. 4c) is due to its single electrode, which limit the total charge transfer and result in lower voltage. For the LS mode and CS mode TENGs (Fig. 4a and d), the FOM$_{RS}$ for the former is smaller than that of the latter. That's because LS mode has larger capacitance than CS mode TENG under the same conditions. The FOM$_{RS}$ calculated for triboelectric process and transient process has been demonstrated in Fig. S8. In addition, from Fig. 4e-f, it can be clearly seen that the ratios of FOM$_{RS}$/FOM$_S$ for LS

mode and CFT mode TENGs are almost constant (both of them are stated at 0.63). Conversely, continuous decline is observed for the other two modes, as depicted in Fig. 4g, and h. Therefore, we can confirm that the structural FOM$_{RS}$ calculated under varied optimum resistances can be used to evaluate the output performance of a certain mode TENG or TENGs with different structures, which are more practical than the FOM$_S$ constructed with the open-circuit and short-circuit processes [35].

Some nonideal effects giving rise to a deviation from the ideal case cannot be neglected [15,23,39]. Studies on these effects are important to investigate the existing model. The first one is the edge effect. Previous work showed the nonideal parallel plate capacitances calculated by considering one side effect is highly consistent with finite element simulation results [35]. Therefore, here the $E_m$ and related FOM$_{RS}$ are all calculated by taking one side effect into account (Supplementary session 5). For instance, the nonideal FOM$_{RS}$ and FOM$_S$ of CS mode TENG are distinctly different with those in the ideal plots shown in Fig. S9. In addition, other design parameters such as the $d_0$ and area size affect the output performance of TENGs, either. The influences of $d_0$ on the FOM$_S$ for CS mode and LS mode TENG, and the gap distance ($g$) and area size (represented by the length $l$) on the SEC mode TENG are systematically studied, as shown in Fig. S10a-d (detailed parameters are listed in Table S3). Besides, the needed time during the four steps, representing by $T_1$, $T_2$, $T_3$ and $T_4$, respectively, are demonstrated in Fig. S11. A rising trend of time at the steps I and III is observed, which is mainly due to the increase of $x_{max}$. At the transient process, five time constants are needed, which can be calculated by the Eqs. (5) and (6). Either the $R$ or $x_{max}$ increases, more time is needed for charges to transfer.

The output characteristics of the four basic modes of TENG under infinitely large and optimum resistances at various $x_{max}$ are shown in Fig. 5. From the basic electrodynamics theory, the open circuit voltage ($V_{xmax}$, when $x = x_{max}$) and the optimum resistance ($R_{opt}$) are strongly influenced by the $x_{max}$. For example, if the $x_{max}$ increases, both the
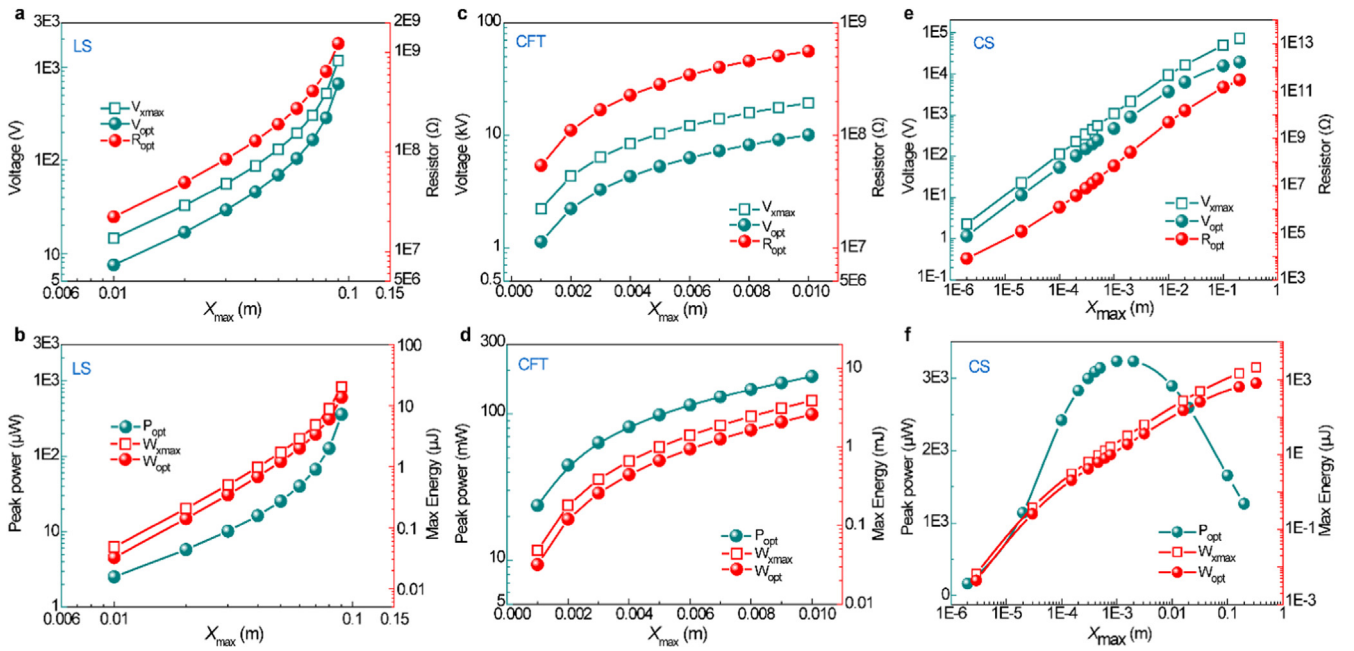
**Fig. 5.** Influence of the maximum displacement $x_{max}$ on the open circuit voltage ($V_{xmax}$), optimum resistance ($R_{opt}$) and corresponding voltage ($V_{opt}$) for (a) LS mode TENG, (c) CFT mode TENG and (e) CS mode TENG. Influence of the maximum displacement $x_{max}$ on the maximum harvested energy under infinitely large load resistance ($W_{xmax}$), the peak power ($P_{opt}$) and corresponding maximum harvested energy ($W_{opt}$) under optimum resistance for (b) LS mode TENG, (d) CFT mode TENG and (f) CS mode TENG.

$V_{xmax}$ and $R_{opt}$ increase. In particular, any parameters that will decrease the inherent capacitance of TENGs will heighten the impedance and thus heighten the $R_{opt}$. Then the alternating current component of $V_{xmax}$ applied to $R_{opt}$ also increases, leading to a large voltage ($V_{opt}$) (Fig. 5a, c, e and Fig. S12a) [22]. On the other hand, when $x_{max}$ becomes larger, the total transferred charges will increase. As a result, both the $W_{xmax}$ and $W_{opt}$ (represent the maximum harvested energy at the infinitely large and optimum resistance, respectively) become larger (Fig. 5b, d, f, and Fig. S12b). Moreover, it is seen that the trends of the $P_{opt}$ are very consistent with those of the $R_{opt}$ for the LS mode and CFT mode TENG. However, for the other two modes, the optimum $x_{max}$ of 0.001 m (for the CS mode) and 0.03 m (for the SEC mode) are observed to generate the maximum $P_{opt}$. Finally, we find that the FOM$_{RS}$ of the LS mode TENG keep the same value when the frequency changes from 1E-4–100 Hz, which further confirms that the FOM$_{RS}$ and the FOM$_S$ are independent of the operation frequency, as depicted in Fig. S13.

Comparisons are carried out between our numerical calculations and the previous published experimental data by Silva et al. [14] and Niu et al. [17], as shown in Fig. S14 (device parameters are presented in Table S4). Fig. S14a shows the profile of peak power with load resistances at different film thicknesses and gap distances for a CS mode TENG. It can be seen in Fig. S14b that the calculated $R_{opt,cal}$ and $P_{opt,cal}$ are slightly higher than the $R_{opt,exp}$ and $P_{opt,exp}$ extracted from experimental results. The similar change tendency can be also found in Fig. S14c, in which the FOM$_{RS}$ are calculated by Eq. (7). The slight mismatch in the predictions and expremental results may be due to the edge effects and parasitic capacitance, which was not possible to be accounted for with the given information. Although these theoretical models have been developed, each of them has its own advantages and disadvantages.

## 3. Conclusion

In summary, the structural figure of merits (FOMs) for TENGs are studied with considering the presence of load resistances, for the four basic modes of TENG. Firstly, to clarify how the charges transfer and the working mechanism of TENGs, we introduce the triboelectric process and transient process in each half cycle. Then one operation cycle of TENGs can be devided into four steps, which corresponds to four first-order ordinary differential equations. After solving these equations, the real-time output characteristics of TENGs in a whole cycle are systematically demonstrated, enabling an in-depth understanding of their working principles. In addition, through the integral of instantaneous power in each step, we numerically calculate the largest possible ourput energy $E_m$, and then the related structural FOM$_S$ with different load resistances are derived to evaluate each TENG structure. More importantly, the influences of various $x_{max}$ on the $R_{opt}$, $P_{opt}$, $W_{opt}$ as well as corresponding FOM$_{RS}$ are also investigated in detail, which provides a theoretical predicting of the key parameters affecting the energy ourput of TENGs. With the viable strategy for in-depth understanding the working principle and calculating the more practical FOM$_{RS}$ of TENGs, we anticipate that the TENGs could be designed more reasonably and utilized more effectively towards a competitive energy scavenging source in the future.

## 4. Methods

The first-order ordinary differential equation was built up through constructing circuit model for the basic mode of TENG, which is given as:

$$R\frac{dQ}{dt} = -\frac{Q}{C(x(t))} + V_{OC}\left(x(t)\right) \tag{12}$$

As triggered by a periodic mechanical force, the triboelectric layer moves back and forth, producing an alternating current. One operational cycle can be divided into four parts, and the circuit variables from each part can be described by a first-order differential equation, thus four different governing equations were built up. To solve these equations, specific boundary conditions should be applied for them. In general, we derive the expression for the first step and then use its solutions as the initial conditions for the next step. Taking the LS mode TENG as an example, at the first step, the boundary condition is $Q$ (t = 0) = 0, and that for the step II is $Q$ (t = $x_{max}/v$) = $Q_0$, where the $Q_0$ can be calculated by assigning $t$ equals to $x_{max}/v$ into Eq. (1). The

same approaches could be used to solve those equations at the second half cycle (Supplementary information 1).

To be closer to the real conditions, we utilize a sinusoidal motion with the following *x-t* relation, (Supplementary information 2)

$$x(t) = \frac{x_{max}}{2}\left[1 - \cos\left(\frac{\pi vt}{x_{max}}\right)\right]$$

(13)

According to our previous researches, for a nonideal parallel plate capacitor, its capacitance value considering one side edge effect can be calculated by the analytical formula, which is listed below [16,35]: (Supplementary information 3)

$$C_s = \varepsilon_0\varepsilon_r\left\{\frac{lw}{d} + \frac{l}{d}\left[1 + \ln\left(1 + 2\pi\frac{w}{d} + \ln\left(1 + 2\pi\frac{w}{d}\right)\right)\right]\right\}$$

(14)

## Acknowledgements

## Appendix A. Supporting information

Supplementary data associated with this article can be found in the online version at doi:10.1016/j.nanoen.2018.07.032.

## References

[1] R.J. Vandegraaff, J.G. Trump, W.W. Buechner, Electrostatic generators for the acceleration of charged particles, Rep. Prog. Phys. 11 (1947) 1–18.

[2] R.G. Horn, D.T. Smith, A. Grabbe, Contact electrification induced by monolayer modification of a surface and relation to acid-base interactions, Nature 366 (1993) 442–443.

[3] H.T. Baytekin, A.Z. Patashinski, M. Branicki, B. Baytekin, S. Soh, B.A. Grzybowski, The mosaic of surface charge in contact electrification, Science 333 (2011) 308–312.

[4] F.R. Fan, Z.Q. Tian, Z.L. Wang, Flexible triboelectric generator, Nano Energy 1 (2012) 328–334.

[5] A. Li, Y. Zi, H. Guo, Z.L. Wang, F.M. Fernandez, Triboelectric nanogenerators for sensitive nano-coulomb molecular mass spectrometry, Nat. Nanotechnol. 12 (2017) 481–487.

[6] Z.L. Wang, New wave power, Nature 542 (2017) 159–160.

[7] H. Ryu, J.H. Lee, T.Y. Kim, U. Khan, J.H. Lee, S.S. Kwak, H.J. Yoon, S.W. Kim, High performance triboelectric nanogenerators based on solid polymer electrolytes with asymmetric pairing of ions, Adv. Energy Mater. 7 (2017) 1700289.

[8] C. Yao, X. Yin, Y. Yu, Z. Cai, X. Wang, Chemically functionalized natural cellulose materials for effective triboelectric nanogenerator development, Adv. Funct. Mater. 27 (2017) 1700794.

[9] J.W. Lee, H.J. Cho, J. Chun, K.N. Kim, S. Kim, C.W. Ahn, I.W. Kim, J.Y. Kim, S.W. Kim, C. Yang, J.M. Baik, Robust nanogenerators based on graft copolymers via control of dielectrics for remarkable output power enhancement, Sci. Adv. 3 (2017) e1602902.

[10] Y. Bao, R. Wang, Y. Lu, W. Wu, Lignin biopolymer based triboelectric nanogenerators, APL Mater. 5 (2017) 074109.

[11] S. Matsusaka, H. Maruyama, T. Matsuyama, M. Ghadiri, Triboelectric charging of powders, Chem. Eng. Sci. 65 (2010) 5781–5807.

[12] J.H. Kim, J. Chun, J.W. Kim, W.J. Choi, J.M. Baik, Self-powered, room temperature electronic nose based on triboelectrification and heterogeneous catalytic reaction, Adv. Funct. Mater. 25 (2015) 7049–7055.

[13] Z.L. Wang, On Maxwell's displacement current for energy and sensors: the origin of nanogenerators, Mater. Today 20 (2017) 74–82.

[14] R.D.I.G. Dharmasena, K.D.G.I. Jayawardena, C.A. Mills, J.H.B. Deane, J.V. Anguita, R.A. Dorey, S.R.P. Silva, Triboelectric nanogenerators: providing a fundamental framework, Energy Environ. Sci. 10 (2017) 1801–1811.

[15] S.M. Niu, Y. Liu, S. Wang, L. Lin, Y.S. Zhou, Y. Hu, Z.L. Wang, Theory of sliding-mode triboelectric nanogenerators, Adv. Mater. 25 (2013) 6184–6193.

[16] S.M. Niu, Y. Liu, S.H. Wang, L. Lin, Y.S. Zhou, Y.F. Hu, Z.L. Wang, Theoretical investigation and structural optimization of single-electrode triboelectric

[17] S.M. Niu, S.H. Wang, L. Lin, Y. Liu, Y.S. Zhou, Y.F. Hu, Z.L. Wang, Theoretical study of contact-mode triboelectric nanogenerators as an effective power source, Energ. Environ. Sci. 6 (2013) 3576–3583.

[18] S. Niu, Y. Liu, X. Chen, S. Wang, Y.S. Zhou, L. Lin, Y. Xie, Z.L. Wang, Theory of freestanding triboelectric-layer-based nanogenerators, Nano Energy 12 (2015) 760–774.

[19] K.Y. Lee, J. Chun, J.H. Lee, K.N. Kim, N.R. Kang, J.Y. Kim, M.H. Kim, K.S. Shin, M.K. Gupta, J.M. Baik, S.W. Kim, Hydrophobic sponge structure-based triboelectric nanogenerator, Adv. Mater. 26 (2014) 5037–5042.

[20] Y. Zi, J. Wang, S. Wang, S. Li, Z. Wen, H. Guo, Z.L. Wang, Effective energy storage from a triboelectric nanogenerator, Nat. Commun. 7 (2016) 10987.

[21] W. Xu, L.B. Huang, M.C. Wong, L. Chen, G. Bai, J. Hao, Environmentally friendly hydrogel-based triboelectric nanogenerators for versatile energy harvesting and self-powered sensors, Adv. Energy Mater. 7 (2017) 1601529.

[22] S. Niu, Y.S. Zhou, S. Wang, Y. Liu, L. Lin, Y. Bando, Z.L. Wang, Simulation method for optimizing the performance of an integrated triboelectric nanogenerator energy harvesting system, Nano Energy 8 (2014) 150–156.

[23] K. Dai, X. Wang, S. Niu, F. Yi, Y. Yin, L. Chen, Y. Zhang, Z. You, Simulation and structure optimization of triboelectric nanogenerators considering the effects of parasitic capacitance, Nano Res. 10 (2017) 157–171.

[24] G. Zhu, J. Chen, T. Zhang, Q. Jing, Z.L. Wang, Radial-arrayed rotary electrification for high performance triboelectric generator, Nat. Commun. 5 (2014) 3426.

[25] J.J. Shao, W. Tang, T. Jiang, X.Y. Chen, L. Xu, B.D. Chen, T. Zhou, C.R. Deng, Z.L. Wang, A multi-dielectric-layered triboelectric nanogenerator as energized by corona discharge, Nanoscale 9 (2017) 9668–9675.

[26] B. Meng, W. Tang, Z.H. Too, X. Zhang, M. Han, W. Liu, H.X. Zhang, A transparent single-friction-surface triboelectric generator and self-powered touch sensor, Energ. Environ. Sci. 6 (2013) 3235–3240.

[27] S. Niu, Y. Liu, Y.S. Zhou, S. Wang, L. Lin, Z.L. Wang, Optimization of triboelectric nanogenerator charging systems for efficient energy harvesting and storage, IEEE Trans. Ind. Electron. 62 (2015) 641–647.

[28] Y. Song, X. Cheng, H. Chen, J. Huang, X. Chen, M. Han, Z. Su, B. Meng, Z. Song, H. Zhang, Integrated self-charging power unit with flexible supercapacitor and triboelectric nanogenerator, J. Mater. Chem. A 4 (2016) 14298–14306.

[29] K.M.A. Šutka, A. Linarts, M. Timusk, V. Jurķāns, I. Gorņevs, J. Blūms, A. Bērziņa, U. Joost, M. Knite, Inversely polarised ferroelectric polymer contact electrodes for triboelectric-like generators from identical materials, Energy Environ. Sci. (2018) https://doi.org/10.1039/C8EE00550H.

[30] J. Chen, H. Guo, X. He, G. Liu, Y. Xi, H. Shi, C. Hu, Enhancing performance of triboelectric nanogenerator by filling high dielectric nanoparticles into sponge pdms film, ACS Appl. Mater. Interfaces 8 (2016) 736–744.

[31] G. Zhu, J. Chen, Y. Liu, P. Bai, Y.S. Zhou, Q. Jing, C. Pan, Z.L. Wang, Linear-grating triboelectric generator based on sliding electrification, Nano Lett. 13 (2013) 2282–2289.

[32] Y. Yang, H. Zhang, J. Chen, Q. Jing, Y.S. Zhou, X. Wen, Z.L. Wang, Single-electrode-based sliding triboelectric nanogenerator for self-powered displacement vector sensor system, ACS Nano 7 (2013) 7342–7351.

[33] Z.L. Wang, Triboelectric nanogenerators as new energy technology and self-powered sensors - Principles, problems and perspectives, Faraday Discuss. 176 (2014) 447–458.

[34] S. Wang, Y. Xie, S. Niu, L. Lin, Z.L. Wang, Freestanding triboelectric-layer-based nanogenerators for harvesting energy from a moving object or human motion in contact and non-contact modes, Adv. Mater. 26 (2014) 2818–2824.

[35] Y. Zi, S. Niu, J. Wang, Z. Wen, W. Tang, Z.L. Wang, Standards and figure-of-merits for quantifying the performance of triboelectric nanogenerators, Nat. Commun. 6 (2015) 8376.

[36] J. Peng, S.D. Kang, G.J. Snyder, Optimization principles and the figure of merit for triboelectric generators, Sci. Adv. 3 (2017) eaap8576.

[37] S. Niu, Z.L. Wang, Theoretical systems of triboelectric nanogenerators, Nano Energy 14 (2015) 161–192.

[38] J.W. James, Electric Circuits, Prentice Hall, Upper Saddle River, NJ, USA, 2014.

[39] Y. Zi, C. Wu, W. Ding, Z.L. Wang, Maximized effective energy output of contact-separationtriggered triboelectric nanogenerators as limited by air breakdown, Adv. Funct. Mater. 27 (2017) 1700049.

**Jiajia Shao** is currently persuing a Ph.D. in Prof. Zhong Lin Wang's group at Beijing Institute of Nanoenergy and Nanosystems, Chinese Academy of Sciences. His research interests include theoretical and experimental studies on: mechanical energy harvesting by triboelectric nanogenerators and energy storage, self-powered systems, nanogenerator-based sensors.
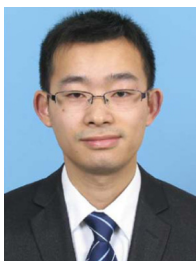
**Tao Jiang** received his Ph.D. degree from East China University of Science and Technology in2014. Now he is an associate researcher in Prof. Zhong Lin Wang's group at the Beijing Institute of Nanoenergy and Nanosystems, Chinese Academy of Sciences. His research interests are the theoretical studies of triboelectric nanogenerators, and practical applications in blue energy harvesting and self-powered sensing.

**Dr. Xiangyu Chen** received his B.S. degree in Electrical Engineering from Tsinghua university in 2007 and his Ph.D. in Electronics Physics from Tokyo Institute of Technology in 2013. Now he is an associate professor in Beijing Institute of nanoenergy and nanosystems, Chinese Academic of Sciences. His main research interests have been focused on the field of organic electronics devices, self-powered nano energy system and the nonlinear optical laser system for characterizing the electrical properties of the devices.

**Wei Tang** received his B.S. degree in the Physics department from Peking University, China, in 2008. He is a Ph.D. candidate at College of Electronic Engineering & Computer Science, in Peking University, from 2008 to 2013. His research interests include nanogenerators and self-powered nanosystem.

**Zhong Lin (Z. L.) Wang** is the Hightower Chair in Materials Science and Engineering and Regents' Professor at Georgia Tech, the chief scientist and director of the Beijing Institute of Nanoenergy and Nanosystems, Chinese Academy of Sciences. His discovery and breakthroughs in developing nanogenerators and self-powered nanosystems establish the principle and technological road map for harvesting mechanical energy from environmental and biological systems for powering personal electronics and future sensor networks. He coined and pioneered the field of piezotronics and piezophototronics.

**Liang Xu** received his Ph.D. degree from Tsinghua University (THU) in 2012, with awards of Excellent Doctoral Dissertation of THU and Excellent Graduate of Beijing. Before that he achieved bachelor's degree of mechanical engineering in Huazhong University of Science & Technology (HUST) in 2007. He is now a postdoctoral fellow at the Beijing Institute of Nanoenergy and Nanosystems, Chinese Academy of Sciences (CAS), under the supervision of Prof. Zhong Lin Wang. His research interests include nanogenerators and self-powered nanosystems, fundamental tribological phenomena, scanning probe microscopy and molecular dynamics simulation.